Bull Volcanol (2006) 68: 641–651
DOI 10.1007/s00445-005-0037-2

RESEARCH ARTICLE

Valerio Lombardo · Maria Fabrizia Buongiorno · Stefania Amici

Characterization of volcanic thermal anomalies by means of sub-pixel temperature distribution analysis

Received: 22 July 2002 / Accepted: 14 September 2005 / Published online: 20 December 2005
© Springer-Verlag 2005

Abstract The simultaneous solution of the Planck equation (involving the widely used "dual-band" technique) using two shortwave infrared (SWIR) bands allows for an estimate of the fractional area of the hottest part of an active lava flow (f_h) and the background temperature of the cooler crust (T_c). The use of a high spectral and spatial resolution imaging spectrometer with a wide dynamic range of 15 bits (DAIS 7915) in the wavelength range from 0.501 to 12.67 μm resulted in the identification of crustal temperature and fractional areas for an intra-crater hot spot at Mount Etna, Italy. This study indicates the existence of a relationship between these T_c and f_h extracted from DAIS and Landsat TM data. When the dual band equation system is performed on a lava flow, a logarithmic distribution is obtained from a plot of the fractional area of the hottest temperature vs. the temperature of the cooler crust. An entirely different distribution is obtained over active degassing vents, where increases in T_c occur without any increase in f_h. This result indicates that we can use scatter plots of T_c vs. fh to discriminate between different types of volcanic activity, in this case between degassing vents and lava flows, using satellite thermal data.

Keywords Mount Etna · Remote-sensing · Dual-band · Lava-flow · Degassing vent · Thermal source

Introduction

Hyperspectral airborne images of the 1996 volcanic eruption of Mt. Etna, located in eastern Sicily, Italy (Fig. 1) were collected using the DAIS 7915 spectrometer (Digital Airborne Imaging Spectrometer) deployed during a multi-sensor campaign of Italian volcanic systems (Horne et al. 1997). We used these data to carry out an analysis of the thermal structures associated with volcanic activity.

Crisp and Baloga (1990) describe the thermal flux for active lava flows as a function of the fractional area of two thermally distinct radiant surfaces: a spatially larger component corresponding to the cooler crust of the flow and a much smaller component related to fractures in the crust. These fractures exhibit a temperature (T_h) assumed to be comparable to the temperature of the molten inner core and that is higher than the crust (T_c). It has been observed that the temperature exposed in hot cracks is 100–200 °C cooler than the molten interior (Flynn et al. 1994; Calvari et al. 1994). This temperature variation for T_h does not affect the results of the presented work since it uses a statistical approach. With this assumption, dual band techniques allow the calculation of T_c and the fractional area of hot cracks (f_h). This sub-pixel temperature retrieval technique (Dozier 1981; Matson and Dozier 1981; Wan and Dozier 1989) requires the availability of a sensor equipped with two bands within the short wave and/or thermal infrared.

This technique has been performed using different sensors characterized by low spatial resolution such as the 1 km^2 data of the advanced very high resolution radiometer (AVHRR; Mouginis-Mark et al. 1994; Harris et al. 1995a, 1997; Harris 1996) and the along track scanning radiometer (ATSR; Wooster and Rothery 1997a,b). In addition it has been applied to Landsat thematic mapper (TM) data, an instrument with a fairly limited dynamic range of 8 bits (Rothery et al. 1988; Glaze et al. 1989; Pieri et al. 1990; Oppenheimer 1991; Flynn et al. 1994; Harris et al. 1998; Wright et al. 2001; Pieri and Buongiorno, 2001 personal communication). The high spatial resolution (30 m per pixel) of TM is important because it increases the number of samples (pixels) available over an active flow. However many pixels located over active lava flows are often saturated in AVHRR and TM data, reducing the number of 'effective' samples available for calculations. In fact, sensors characterized by an 8 bit dynamic range, such as Landsat TM, are badly affected by saturation of radiant

Editorial responsibility: A. Harris

V. Lombardo (✉) · M. F. Buongiorno · S. Amici
Istituto Nazionale di Geofisica e Vulcanologia,
Via di Vigna Murata, 605,
00143 Rome, Italy
e-mail: lombardo@ingv.it
Tel.: +39-06-51860508
Fax: +51860507

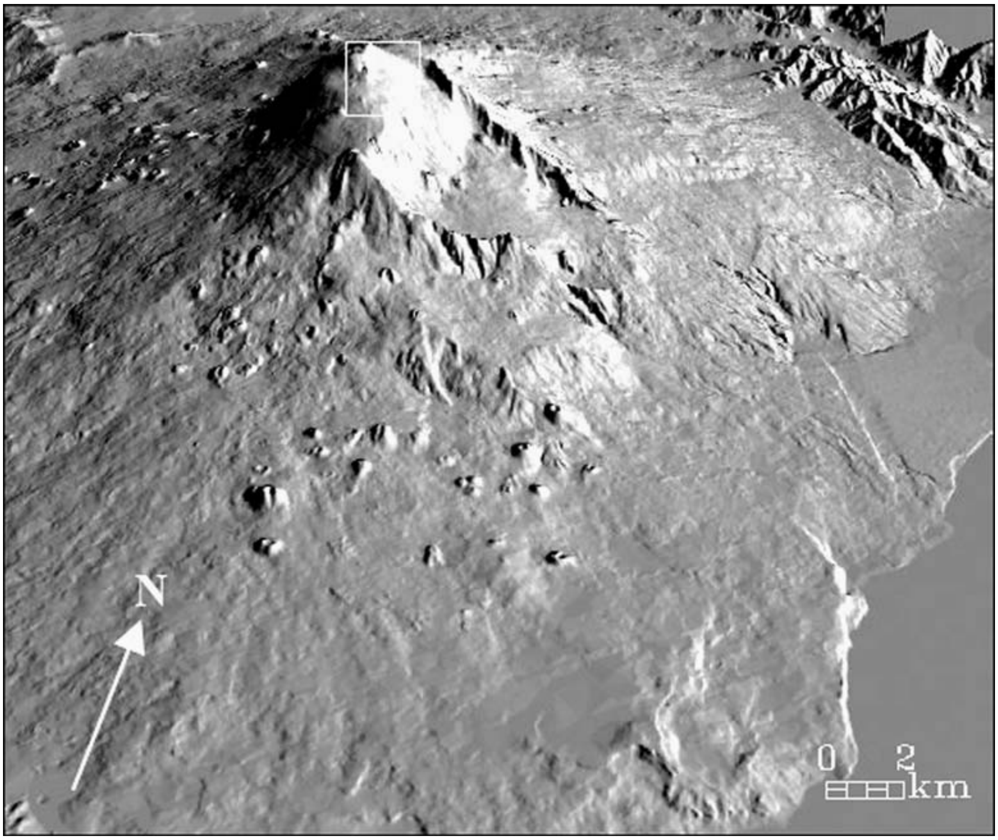

Fig. 1 Location map of Mount Etna: *shaded relief* draped over a three-dimensional image derived from a 10 m resolution digital elevation model (DEM) generated by Istituto Nazionale di Geofisica e Vulcanologia, Italy. A 3× exaggeration of the vertical scale was adopted. The *square box* indicates approximately the area imaged by DAIS (see Fig. 2)

pixels containing active vents or located in the middle of a lava flow (Pieri et al. 1990; Oppenheimer 1991; Rothery et al. 1992; Flynn et al. 2000, 2001). Data saturation makes statistical evaluations of the thermal structures that characterize an active flow complicated.

The high spatial resolution of DAIS data (2–20 m; Table 1), with its 15 bit dynamic range, provides a way to test and develop algorithms on a large number of unsaturated points. This makes DAIS-type data ideally suited to statistical investigations of radiant pixels. In addition, high spatial resolution data enhance the discrimination between the active part of lava flows and the much cooler ground surrounding the lava margins. This reasonably prevents the inclusion of an extra radiative contribution to pixel-integrated temperatures coming from a non-active lava background. Here, we illustrate our statistical approach using two DAIS images obtained on 16 and 18 July, 1996 and coinciding with a phase of summit activity at Mount Etna.

The 1996 Mt. Etna eruptive activity

The eruptive activity at Mount Etna during the 1996 DAIS campaign (Horne et al. 1997) was recorded on two dates, 16 and 18 July. This phase of the activity persisted from 1995 to 1999 and was one of the most complex and long lasting eruptive cycles at Etna of recent times (GVN 1997). Activity began at the Bocca Nuova crater during late July 1995, and was followed by a gradual reactivation of the North-East (NE) crater (Fig. 1). By July 1996, three of the four main summit craters of Mt. Etna (Fig. 1) were active: the North-East, La Voragine and Bocca Nuova (GVN 1996a). Figure 2 shows the locations of the vents and other morphologic features of the summit crater area of Mt. Etna, retrieved from an analysis of the 16 July 1996 (Fig. 2a) and of the 18 July 1996 DAIS images (Fig. 2b).

Activity at the NE crater between July 1995 and July 1998 can be divided into several distinct periods of eruptive behavior. Between mid-February and late-August 1996, persistent Strombolian activity occurred, punctuated by two paroxysmal episodes of fire-fountaining in June 1996 and culminating in four weeks of lava effusion. This intra-crater activity is recognizable in the DAIS images as a zone of highly radiant pixels within the crater. Radiance statistics for pixels associated with this activity are reported in Table 2. The initially weak activity at La Voragine was characterized by an open pit that had been degassing quietly for 2 years (GVN 1996b, 1997). This crater became active only after 1997 when it produced two of the most intense eruptive events of the 1995–1999 period (GVN 1998). The first episode began on June 1998 and lasted 4 months. Explosive activity, lava effusion and scoria emission characterized this eruptive phase. The second episode occurred on 4 September 1999, when a lava fountain rose hundreds of meters above La Voragine and a tephra-laden eruption column rose ~2 km above the vent before being blown eastwards (GVN 1999). However, the only activity at La Voragine during July 1996 when the DAIS data were collected consisted of continuous gas emission. In the DAIS

Table 1 Major characteristics of the DAIS 7915 sensor: *IFOW* Instantaneous Field of View, *GIFOV* Ground projected Instantaneous Field Of View, and detector types (*Si* Silicium, *InSb* Indium-Antimonide, *MCT* Mercury-Cadmium-Telluride), and FWHM for all bands—center wavelength and full width at half maximum value (FWHM) for all bands (spectral calibration results of April 1997)

Technical characteristics of DAIS			
Spectrometer characteristics			
(Wavelength range: 400 nm–12.6 μm, 4 spectrometers, 79 bands)			
(1) 400–1,000 nm: 32 bands, bandwidth = 15–30 nm detector: Si			
(2) 1,500–1,800 nm: 8 bands, bandwidth = 45 nm detector: InSb			
(3) 2,000–2,500 nm: 32 Bands, Bandwidth = 20 nm Detector: InSb			
3,000–5,000 nm: 1 band, bandwidth = 2.0 μm detector: InSb			
(4) 8,000–12,600 nm: 6 bands, bandwidth = 0.9 μm detector: MCT			
Main radiometric parameters			
–dynamic range: 15 bit (no gain settings)			
–sensitivity VIS/NIR:			
NER < 0.025 mW/cm^2 sr μm			
SWIR: NER < 0.025 mW/cm^2 sr μm			
MIR/TIR: NET < 0.1 K			
Main geometric parameters			
FOV: 0.894 rad (±26°)			
IFOV: 3.3 mrad, (0.189°)			
GIFOV: depending on aircraft altitude 2–20 m			
FWHM for all bands			
Spectrometer I, VIS-NIR		Spectrometer III, SWIR-2	
1	0.501, 0.030	41	2.004, 0.040
2	0.517, 0.019	42	2.017, 0.040
3	0.533, 0.018	43	2.032, 0.032
4	0.552, 0.020	44	2.050, 0.032
5	0.567, 0.021	45	2.066, 0.024
6	0.587, 0.020	46	2.085, 0.020
7	0.603, 0.019	47	2.103, 0.020
8	0.621, 0.022	48	2.118, 0.016
9	0.636, 0.020	49	2.135, 0.016
10	0.654, 0.022	50	2.150, 0.016
11	0.671, 0.024	51	2.166, 0.016
12	0.689, 0.023	52	2.183, 0.016
13	0.705, 0.026	53	2.199, 0.016
14	0.722, 0.027	54	2.219, 0.020
15	0.739, 0.027	55	2.236, 0.016
16	0.756, 0.030	56	2.252, 0.020
17	0.773, 0.032	57	2.268, 0.020
18	0.791, 0.031	58	2.284, 0.016
19	0.807, 0.034	59	2.299, 0.024
20	0.825, 0.036	60	2.314, 0.024
21	0.843, 0.037	61	2.328, 0.024
22	0.860, 0.037	62	2.343, 0.028
23	0.877, 0.038	63	2.359, 0.028
24	0.895, 0.038	64	2.374, 0.024
25	0.912, 0.038	65	2.389, 0.024
26	0.930, 0.037	66	2.404, 0.024
27	0.947, 0.037	67	2.420, 0.020
28	0.965, 0.034	68	2.434, 0.020
29	0.985, 0.032	69	2.449, 0.020
30	1.004, 0.036	70	2.462, 0.016
31	1.021, 0.040	71	2.475, 0.016
32	1.034, 0.038	72	2.490, 0.016

Table 1 Continued.

Spectrometer II, SWIR-1		Spectrometer IV, thermal	
33	1.538, 0.059	73	4.37, 2.16
34	1.563, 0.061	74	8.75, 0.85
35	1.591, 0.053	75	9.65, 0.88
36	1.619, 0.049	76	10.48, 0.92
37	1.650, 0.045	77	11.27, 1.07
38	1.678, 0.041	78	12.00, 1.38
39	1.705, 0.037	79	12.67, 1.54
40	1.729, 0.037		

data there were 52 radiant pixels related to this activity, of which none were saturated (Table 2).

During the first two years of the 1996–1999 eruptive cycle, activity within the Bocca Nuova crater was moderate, resulting in a slow filling of the crater by intra-crater cones and lava flows (GVN 1996a). The eruption of lava within the crater was occasionally accompanied by gaseous emissions from fumaroles scattered around the intra-crater. Radiant pixels occur in two zones within the Bocca Nuova crater: (1) a circular zone, including some saturated pixels, in the center of the crater and (2) a zone scattered in the southern part of the crater (Fig. 2). Saturated pixels only occur in the central zone of 208 pixels (Table 2).

Data reduction

The DAIS instrument consists of four spectrometers known as VIS-NIR, SWIR-1, SWIR-2 and thermal, covering a spectral range of 0.4–12.6 μm for a total of 76 bands (see Table 1 for more details). To constrain lava temperatures, we consider spectrometers II (SWIR-1) and III (SWIR-2). These sensors are equipped with 37 bands in the 1.54–2.49 μm range. These are suitable for dual band style calculations (Rothery et al. 1988). Unfortunately, not all the bands could be used in the dual band equations because of strong noise contamination, especially in the SWIR-1 data across the 1.54–1.73 μm wavelength range .

The dual band system equation adapted for the DAIS bands can be summarized as follows (e.g. Rothery et al. 1988):

$$R\alpha = f_{\rm h}(R_{\rm h}\alpha) + (1 - f_{\rm h})R_{\rm c}\alpha$$
$$R\beta = f_{\rm h}(R_{\rm h}\beta) + (1 - f_{\rm h})R_{\rm c}\beta \qquad (1)$$

where R_α and R_β are respectively the total radiance in two suitable bands (α and β) and $R_{\rm h}\alpha$ and $R_{\rm h}\beta$ are the radiance values calculated for the same bands using the Planck equation with 1,080 °C as the hot temperature ($T_{\rm h}$) for Etna lavas (GVN 1996a, 1999; Calvari et al. 1994; Archambault and Tanguy 1976; Gauthier 1973). The simultaneous solution of the equations now allows for the calculation of the fractional area of the hottest component $f_{\rm h}$, as well as the cooler crust temperature $T_{\rm c}$. In applying Eq. (1), our aim was to obtain $T_{\rm c}$ and $f_{\rm h}$ for every pixel across the thermal anomaly.

Previous results achieved from Landsat TM imagery

The bands used in Eq. (1) were selected to allow a comparison between our new results and the previous results achieved at Etna using Landsat TM data (Lombardo et al. 2004). The DAIS bands used for the dual band calculations were thus selected so that they were as close as possible to the corresponding SWIR bands of the Landsat TM. These are TM bands 5 and 7, corresponding to central wavelengths of 1.65 and 2.22 μm, respectively. The DAIS

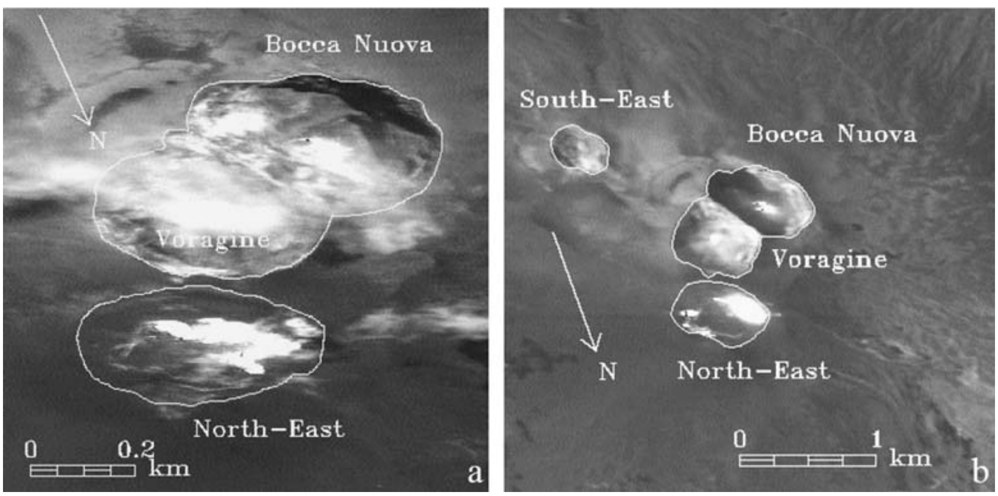

Fig. 2 **a** Location of the vents and morphological features of the craters as revealed by band 36 (1.62 μm) of the 16 July 1996 DAIS image. Flight altitude is 4,000 m corresponding to a ground resolution of 2.3 square meters. **b** Location of the vents and morphological features of the craters detected by band 36 of the 18 July 1996 DAIS image. Flight altitude is 6,000 m corresponding to a ground resolution of 8.9 m^2

Table 2 Statistics for saturated pixels in the DAIS imagery obtained for each hot spot

Target	Pixels sampled	Pixel saturated at 1.619 μm	Pixel saturated at 2.199 μm	Mean intensity at 1.619 μm ($mW\ m^{-2}\ sr^{-1}\ \mu m^{-1}$)	Mean intensity at 2.199 μm ($mW\ m^{-2}\ sr^{-1}\ \mu m^{-1}$)
NE 16 July 1996	2,933	123	248	35,412	67,642
Voragine 16 July 1996	52	0	0	19,012	53,536
Bocca Nuova 16 July 1996	810	33	38	11,572	20,249
NE 18 July 1996	1726	102	157	11,188	27,462
Voragine18 July 1996	113	0	6	8,143	32,804
Bocca Nuova 18 July 1996	42	9	14	29,630	74,117

Note. From left to right the columns show: number of radiant pixels which provide solutions from the dual-band calculation, number of pixels saturated in bands 1.619 and 2.199 μm, and mean intensity of the radiant pixels in band 1.619 and 2.199 μm ($mW\ m^{-2}\ ster^{-2}\ \mu m^{-2}$)

instrument provides two bands (band 37 and 54, Table 1) that fall within the same wavelength region as TM bands 5 and 7. Unfortunately DAIS band 37 (1.650 μm) is one of the bands affected by noise, having an extremely poor signal to noise ratio. For this reason band 36 (1.619 μm) was preferred in the solution of the dual-band equations.

The statistics derived from our Landsat TM results (Lombardo et al. 2004) show a recurring trend when we plot f_h vs. T_c for distinct eruptive events. A logarithmic curve provides the best fit for this distribution of points (Lombardo et al. 2004). This trend shows a systematic increase in f_h as T_c increases. Such a positive relationship is consistent with a lava-flow surface structure where larger areas of the exposed hot core often occur when the crust temperature is higher (i.e., more active flows).

Statistics for saturated pixels in our Landsat data are reported in Table 3. The percentage of unsaturated pixels available to perform the dual band system equation, and thus the calculation of T_c and f_h, ranges from 59 to 29 percent. The total number of non-saturated pixels varies from 41 to 1,428; the upper value corresponding to data collected when a large lava field was active within Valle del Bove during 1992. In comparison, the average number of non-saturated pixels available for all the other eruptions is about 220 (Table 3). We can compare these statistics with a value of 95% for the percentage of unsaturated pixels available from the 16 July 1996 DAIS image. This corresponds to a total number of 2,933 unsaturated pixels. The lower spatial resolution (30 by 30 m) and limited dynamic range (8 bits) of Landsat TM data accounts for this difference.

Data analysis

We analyzed the scatter plots of derived crust temperature T_c vs. the hot crack fractional area f_h for each of the intra-crater hot zones identified in Fig. 2. We found that each distribution revealed a similar trend and matched the expected thermal structure fingerprint for active lava. Figure 3a displays a logarithmic trend linking T_c and f_h for the unsaturated pixels of the 16 July 1996 lava flow that erupted onto the floor of the NE crater. This distribution thus shows a trend that can be summarized as follows. Between T_c of 0 and approximately 160 °C, increases in T_c occur without a significant increment in the fractional area of the hot crack. With higher values of T_c (>160 °C), f_h increases exponentially so that small variations in T_c correspond to a proportionally larger increment in the fractional area. Figure 3b shows the same data plotted on a log scale, confirming the logarithmic relationship between T_c and f_h. This plot reveals that the derived data lie along a line with a very narrow dispersion range. This trend is expressed by:

$$T_c = 61\ \ln(f_h) + 652 \tag{2}$$

with an R^2 of 0.67.

The logarithmic trend observed in our DAIS data (Fig. 3a) is comparable to the plot derived from the Landsat imagery. However, the relationship defined using Landsat TM data

Table 3 Statistics for saturated pixels in the time series of Landsat TM images analyzed by Lombardo et al. (2004)

Acquisition date	Total number of radiant pixels	Dual-band solvable		Dual-band solvable		Saturated pixels in band 7 & 5	
	Pixel	Pixel	%	Pixel	%	Pixel	%
TM 1984-05-19	333	135	41	198	59	91	27
TM 1984-06-20	336	136	40	200	60	98	29
TM 1984-09-24	243	137	56	106	44	34	14
TM 1985-04-04	471	252	54	219	46	99	21
TM 1985-06-23	493	189	38	304	62	151	31
TM 1992-01-02	435	227	52	208	48	99	23
TM 1992-02-03	2668	1428	54	1240	46	687	26
TM 1992-05-09	1042	450	43	592	57	276	26
TM 1992-07-12	319	91	29	228	71	281	88
TM 1992-08-13	748	411	55	337	45	103	14
TM 1992-08-29	277	137	49	140	51	94	34
TM 1992-09-30	722	426	59	296	41	101	14
Average			48		52		29

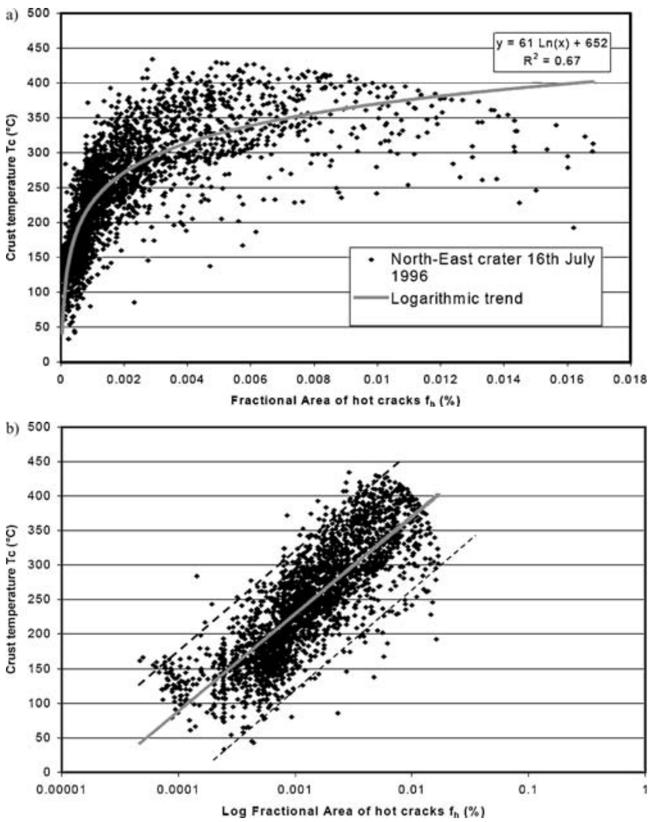

Fig. 3 **a** Arithmetic and **b** logarithmic plot of T_c vs. f_h for the North-East crater hot-spot obtained from the 16 July 1996 DAIS image. *Dashed lines* in logarithmic plot identify typical scatter about the best-fit trend line (*gray*)

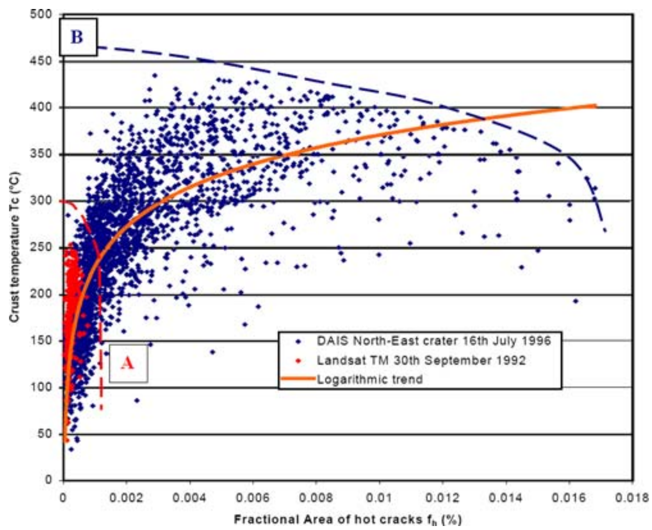

Fig. 4 Plot of T_c vs. f_h derived from the 30 September 1992 Landsat TM image (*red dots*) and the 16 July 1996 DAIS data (*blue dots*). We use these scatter distributions to compare the effect of the dynamic range on T_c and f_h solutions. We observe that saturation in TM data (*A curve*) occurs at a lower level than DAIS data (*B curve*)

is incomplete. This is due to the inferior dynamic range of the TM sensor, which produces saturation at lower temperatures and causes the high-temperature limb of the relationship to be clipped (Fig. 4). Figure 4 shows a plot of T_c vs. f_h obtained using the 30 September 1992 Landsat image in the 0–250°C temperature range. It is easy to recognize the same trend shown in Fig. 3a.

A comparison of these two plots (Fig. 4) is instructive in understanding how the dynamic range affects the dual-band technique. The most relevant detail is that the 15-bit DAIS data allows solution for a wider range of T_c. Indeed, the T_c upper limit for Landsat TM data is one half (about 250 °C) of the DAIS T_c upper limit of 450 °C. It follows that it is impossible to entirely determine the full relationship between T_c and f_h, using Landsat TM data alone.

Figure 5a and b map the derived crust temperatures and fractional areas respectively, obtained for the 16 July 1996 DAIS image. The spatial distribution of T_c in the NE crater (Fig. 5a) shows a concentric arrangement. Cooler values are located along the lava boundaries while the hottest pixels are prevalent at the center of the anomaly. These results relate to a ground-based situation in which a lava pond was present (GVN 1996a). This is not to be confused with an active lava lake which forms directly on top of the magma column (Swanson et al. 1979). Effusive activity recorded at the NE crater consisted in a ponding of lava that was trapped in the topographic low (GVN 1996a). Degassing from the

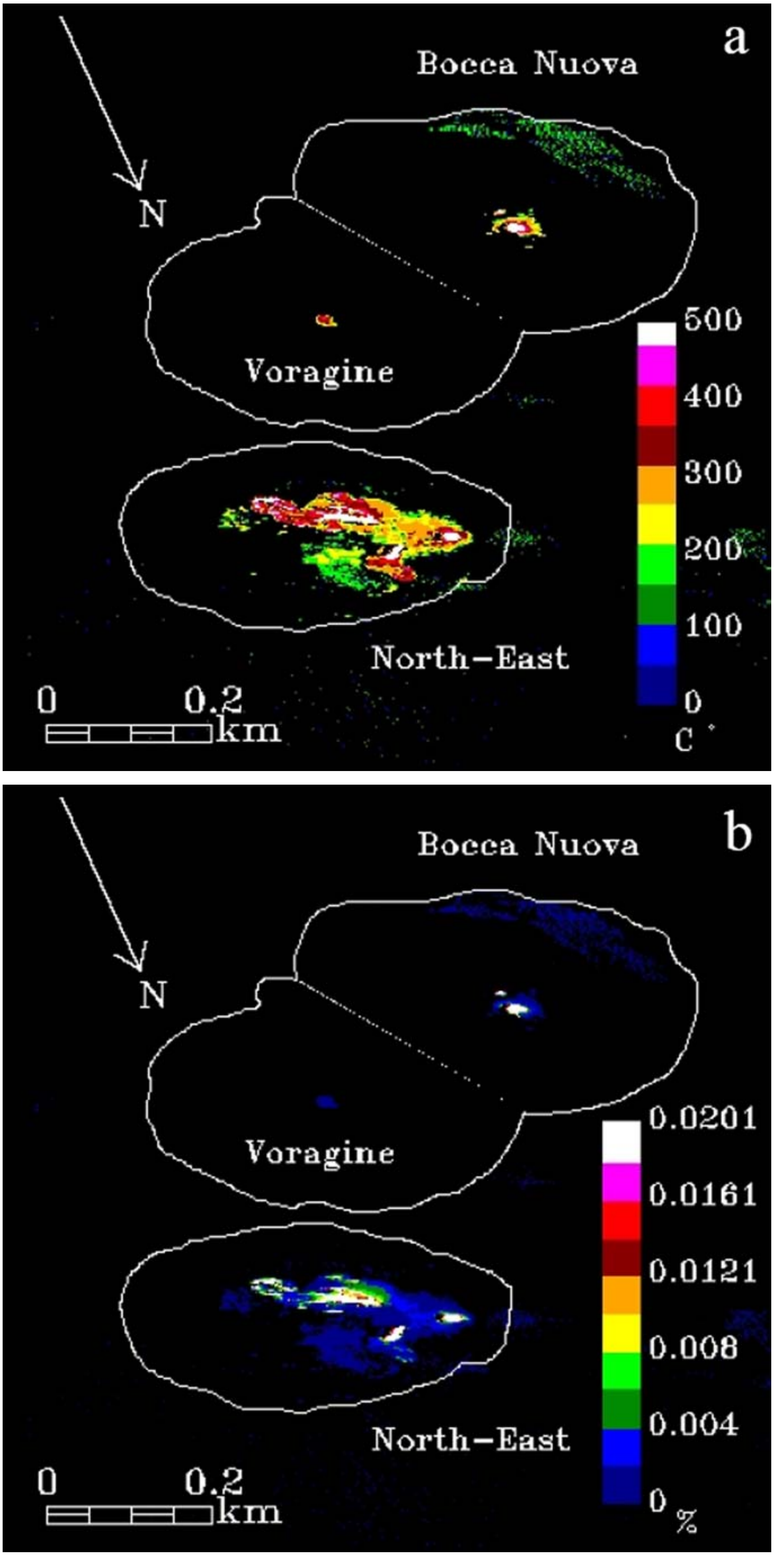

Fig. 5 **a** Crust temperature T_c and **b** fractional area f_h spatial distributions obtained using the dual band technique with the 16 July 1996 DAIS image. **c** Location of two spatial profiles taken across the North-East crater

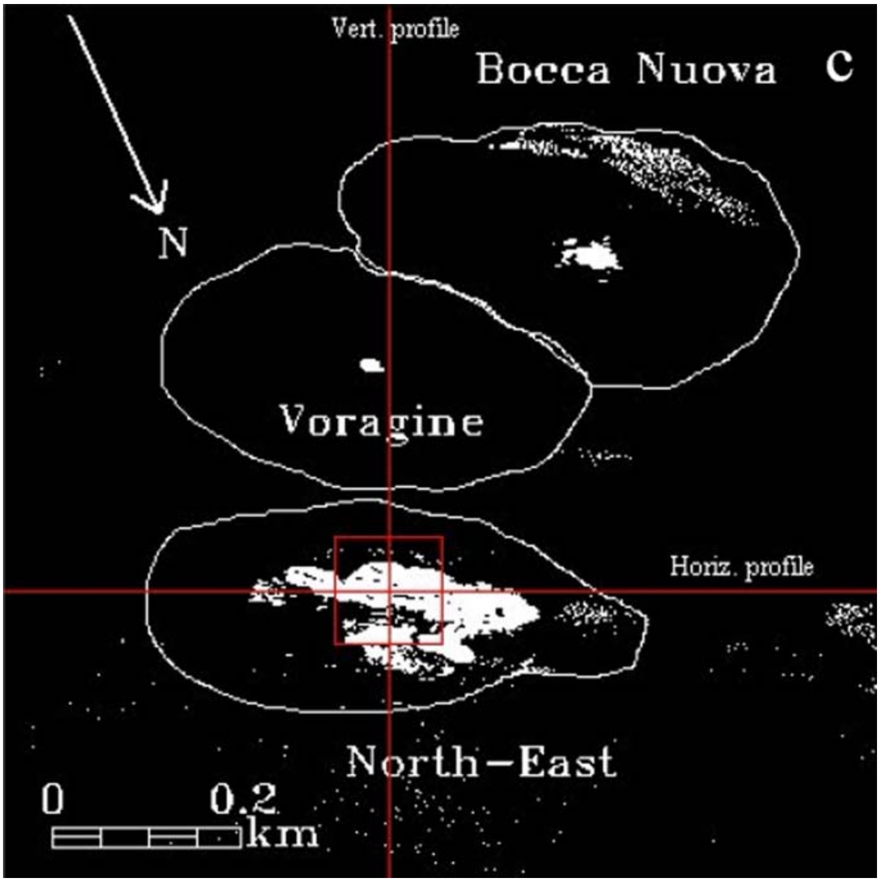

Fig. 5 Continued.

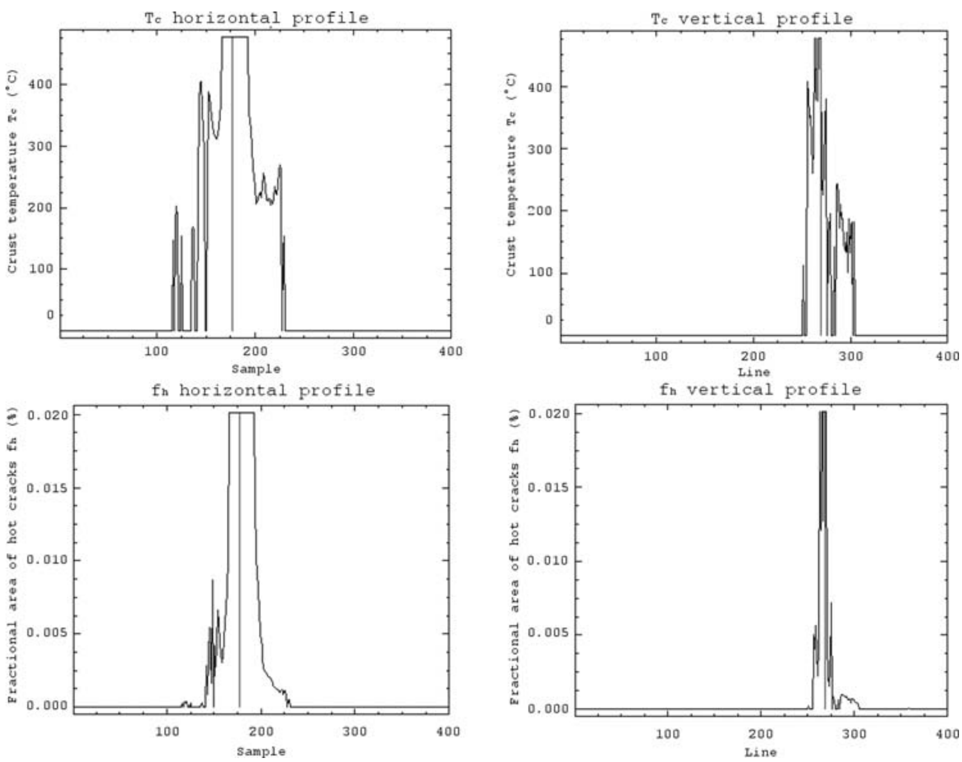

Fig. 6 Crust temperature T_c and fractional area f_h profiles (horizontal and vertical) across the NE crater hot spot on the 16 July image (Fig. 5)

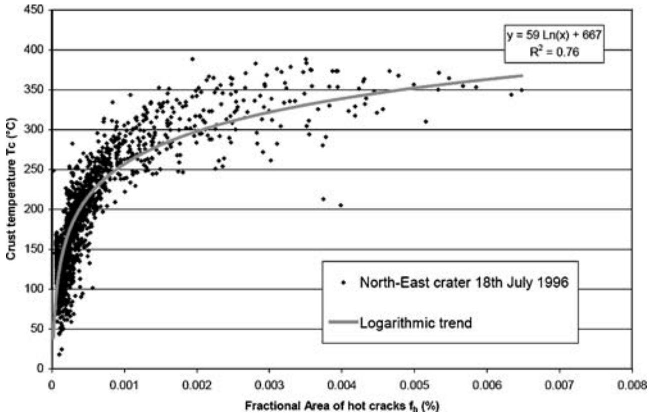

Fig. 7 T_c vs. f_h plot for the North-East crater hot-spot on the 18 July 1996 DAIS image and logarithmic interpolation

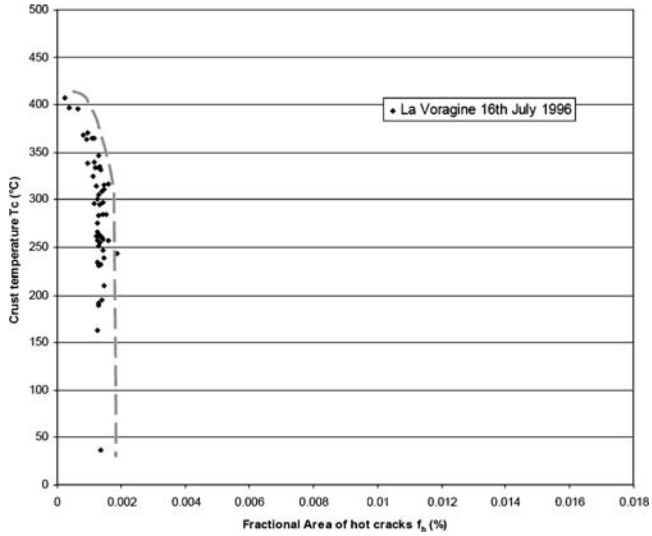

Fig. 8 T_c vs. f_h distribution and observed trend (dashed line) for La Voragine crater hot spot in the 16 July 1996 DAIS image

vent beneath the pond will cause disruption of the surface crust at the feature center and would thus explain the spatial distribution of T_c and f_h observed by us for this case. Also, the fractional area occupied by the cracks increases from the periphery to the center of the ponds with highest values of f_h occurring at feature center (Fig. 5b).

Figure 6 shows spatial profiles of T_c and f_h across the NE crater lava pond (see Fig. 5c for profile locations). These exhibit a rapid increase of T_c when moving from the edge to the feature center, which is not matched by a proportional increment in f_h, which tends to vary at a slower rate. Approaching the middle of the lava body, however, f_h begins to increase rapidly so that T_c and f_h reach their maxima at the same central location.

Similar results are obtained from the 18 July 1996 DIAS image. Compared to the 16 July image, the percentage of unsaturated pixels is higher (91%) but the total number of radiant pixels is lower (1,726). This is related to the lower spatial resolution of 8.9 m due to the higher flight altitude of 6,000 m adopted for the 18 July 1996 acquisition. The 16 July flight altitude was 4,000 m, corresponding to a ground resolution of 2.3 m. The 18 July image is useful because it allows for the comparison between results achieved with different spatial resolution data. In this regard, the 18 July results for the NE crater (Fig. 7) shows a similar distribution of T_c vs. f_h to that obtained on 16 July. Once more, the relationship is logarithmic, with a best fit of:

$$T_c = 59\ \ln(f_h) + 667 \quad \text{and} \quad R^2 = 0.76. \tag{3}$$

The T_c vs. f_h distribution obtained for the 18 July hot spot within La Voragine, however, is entirely different. Below T_c of 350 °C, the distribution of points falls along a nearly vertical line parallel to the T_c axis (Fig. 8). This means that over this temperature range, f_h remains constant with increasing T_c. For T_c greater than 350 °C, however, increasing T_c are associated with decreasing f_h. This trend is entirely different from the logarithmic distribution encountered for the NE crater (Fig. 7). This different distribution obtained for La Voragine is consistent with ground-based observations (GVN 1996a) that reveal that a degassing vent, rather than an active lava body, was active in La Voragine during July 1996. We can thus infer that our data relate to active degassing vent(s) inside this crater when the image was taken. The typical range of temperatures given for the degassing feature in Fig. 8 is 50–400 °C. This range is comparable with the T_c range obtained for the lava feature given in NE crater (Fig. 3). Table 4 reports maximum, minimum and mean T_c and f_h obtained for each hot spot. These data show that there is no apparent difference in derived T_c between degassing and lava features. Thus, the features cannot be separated on the basis of temperature alone. However, when the features are examined in terms of a scatter plot of T_c vs. f_h, the two features are apparent from their different distribution. This result indicates that we can use the scatter plot of T_c vs. f_h as a method to discriminate between different types of volcanic activity in remotely sensed thermal date.

We examined the 18 July hot spot within Bocca Nuova (BN) in terms of these criteria. The results indicate a mixed situation comprising degassing and lava flow activity. The

Table 4 Maximum, minimum and mean T_c and f_h values derived from DAIS data for each hot spot

Target	T_c max (°C)	T_c mean (°C)	T_c min (°C)	f_h max (%)	f_h mean (%)	f_h min (%)
NE 16 July 1996	477.6	266.5	33.4	1.185×10^{-2}	3.457×10^{-3}	4.7×10^{-5}
Voragine16 July 1996	407.1	286.4	37.1	1.867×10^{-3}	1.255×10^{-3}	2.52×10^{-4}
Bocca Nuova 16 July 1996	457.5	180.4	20.9	2.014×10^{-2}	1.672×10^{-3}	2.0×10^{-6}
NE 18 July 1996	427.8	213.8	15.3	7.504×10^{-3}	1.207×10^{-3}	3.2×10^{-5}
Voragine18 July 1996	444.9	189.6	52.1	2.208×10^{-3}	5.26×10^{-4}	8.2×10^{-5}
Bocca Nuova 18 July 1996	385.5	279.2	101.4	4.65×10^{-3}	2.351×10^{-3}	2.0×10^{-6}

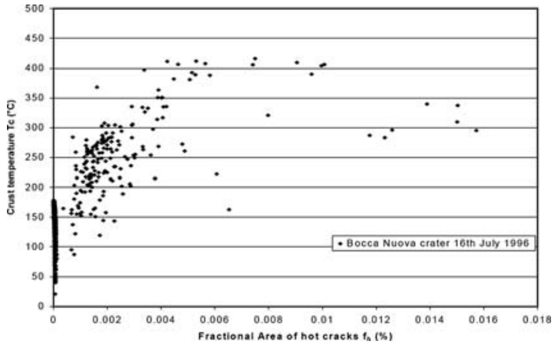

Fig. 9 Plot of T_c vs. f_h for the Bocca Nuova crater hot spot in the 16 July 1996 DAIS image. Note the two apparent trends

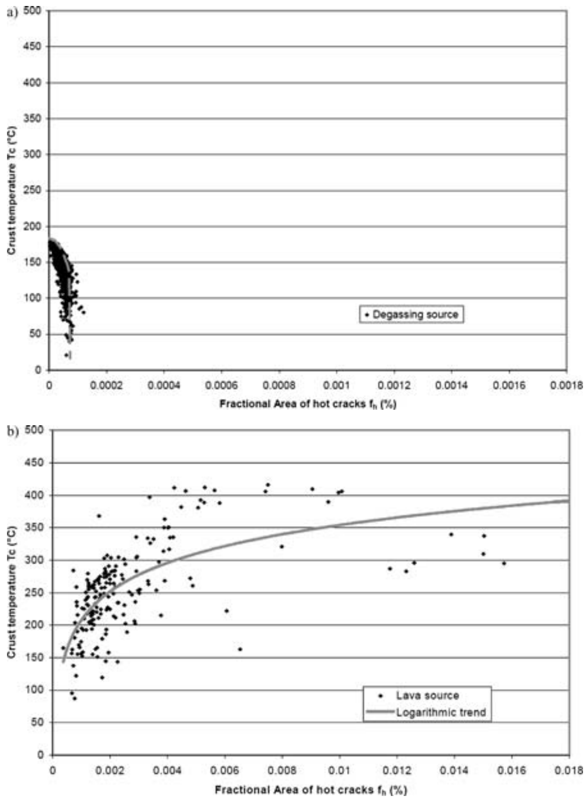

Fig. 10 Plot of T_c vs. f_h for the inferred **a** degassing and **b** lava components of the *Bocca Nuova* hot-spot

plot of the dual band parameters (Fig. 9) is clearly split into two separate distributions: a linear distribution parallel to the T_c-axis (expanded in Fig. 10a) and a second distribution that approaches the logarithmic relationship found for our lava flow (Fig. 10b). In effect, the analysis of the pure cases at the NE Crater and La Voragine allow these features now to be distinguished at the BN with some confidence; where the first trend indicates the presence of a degassing vent and the second trend indicates an active lava flow.

Conclusions and future work

Our analysis of the parameters calculated using the dual band technique indicates that unique relationships in plots of flow crust temperature, T_c, vs. the fractional area of hot cracks, f_h, allow us to distinguish two different hot volcanic features (lava flows and degassing vents). Finding this relationship was enabled by the use of a high spectral and spatial resolution spectrometer data which has a wide dynamic range of 15 bits, and therefore pixels are rarely saturated. These data attributes allow for a complete analysis of a large number of unsaturated pixels and yield results that are statistically significant. When dual-band solutions are derived for pixels corresponding to an active lava flow or lava pond and assuming a suitable value for the hottest temperature T_h, a logarithmic relationship is obtained from the distribution of T_c vs. f_h. This result is in agreement with the solutions achieved using Landsat TM data for an active lava flow. In contrast, the relationship obtained from pixels containing active degassing vents is entirely different. A sub-vertical trend, parallel to the T_c axis, reveals the presence of a degassing activity.

The next step will be to apply this method to a larger selection of data in order to verify this technique and improve its accuracy. The availability of a large number of images of different active sites in Italy (Mt. Etna, Vulcano, 'Campi Flegrei') characterized by gas emissions will allow for the further testing and refinement of this approach. Then this technique will be suitable to be applied on those sites where field measurements are difficult such as Erebus or Nyragongo. For extra-terrestrial volcanic activity such as the one observed on Jupiter's satellite IO, the presented methodology could be used to discriminate surface thermal features which maybe correlated to lava flows, lava lakes and high temperature degassing vents or fracture.

Acknowledgements We are grateful to Prof. Dieter Oertel, Andreas Muller, Peter Strobl, Han-Ruediger Boehl and Peter Hausknecht of the German Aerospace Research Establishment (DLR) Germany, who have kindly provided us with the DAIS data used in this research. The authors would also like to express their sincere gratitude to Prof. Paul Milton Robicheaux, Director of the John Milton International Language School, Italy, for proof-reading the text which has greatly improved its clarity. Special thanks to the referees, Dr. Harris, Dr. Donegan, and Dr. Rowland for the insightful comments on the manuscript.

References

Archambault C, Tanguy JC (1976) Comparative temperature measurements on Mount Etna lavas: problems and techniques. J Volcanol Geotherm Res 1:113–125

Crisp J, Baloga S (1990) A model for lava flows with two thermal components. J Geophys Res 95:1255–1270

Calvari S, Coltelli M, Neri M, Pompilio M, Scribano V (1994) The 1991–1993 Etna eruption: chronology and geological observations. Acta Vulcanol 4:1–14

Dozier J (1981) A method for satellite identification of surface temperature fields of subpixel resolution. Remote Sensing Environ 11:221–229

Flynn LP, Harris AJL, Rothery DA, Oppenheimer C (2000) High-Spatial resolution thermal remote sensing of active volcanic features using Landsat and hyperspectral data. In: Mouginis-Mark PJ, Crisp JA, Fink JH (eds) Remote sensing of active volcanism, vol 116. AGU Monograph, pp 161–177

Flynn LP, Harris AJL, Wright R (2001) Improved identification of volcanic features using Landsat 7 ETM+. Remote Sensing Environ 78:180–193
Flynn LP, Mouginis-Mark PJ, Horton KA (1994) Distribution of thermal areas on an active lava flow field: Landsat observations of Kilauea, Hawaii, July 1991. Bull Volcanol 56:284–296
Gauthier F (1973) Field and laboratory studies of the rheology of Mount Etna lava. Philos Trans Roy Acad Lond 274:83–98
Glaze L, Francis PW, Rothery DA (1989) Measuring thermal budgets of active volcanoes by satellite remote sensing. Nature 338:144–146
GVN (1996a) Etna. Smithsonian Inst Bull Global Volcanol Net 21(07)
GVN (1996b) Etna. Smithsonian Inst Bull Global Volcanol Net 21(06)
GVN (1997) Etna. Smithsonian Inst Bull Global Volcanol Net 22(07)
GVN (1998) Etna. Smithsonian Inst Bull Global Volcanol Net 23(11)
GVN (1999) Etna. Smithsonian Inst Bull Global Volcanol Net 24(06)
Harris AJL (1996) Low spatial resolution thermal monitoring of volcanoes from space. PhD Thesis, Open University, Milton Keynes, UK
Harris AJL, Blake S, Rothery DA (1997) A chronology of the 1991 to 1993 Mount Etna eruption using advanced very high resolution radiometer data: implication for real-time thermal volcano monitoring. J Geophys Res 102:7985–8003
Harris A, Buongiorno MF, Pieri DC, Rothery RA, Stevens N (1996) Mount Etna: the view from above, in Mt. Etna, 15 years on. In: Gravestock PJ, McGuire WJ (eds) Proceedings of the C&GCHE Volcanic Research Centre Etna Conference, Cheltenham,UK pp 68
Harris AJL, Flynn LP, Dean K, Pilger E, Wooster MJ, Okubo C, Mouginis-Mark PJ, Garbeil H, Thornbern C, De la Cruz-Reyna S, Rothery DA, Wright R (2000a) Real-time monitoring of volcanic hot-spots with satellites. Remote Sensing Active Volcan AGU Geophys Monogr Ser 116:139–159
Harris AJL, Flynn LP, Keszthelyi L, Mouginis-Mark PJ, Rowland SK, Resing JA (1998) Calculation of lava effusion rates from Landsat TM data. Bull Volcanol 60:52–71
Harris AJL, Flynn LP, Rothery DA, Oppenheimer C, Sherman SB (1999) Mass flux measurements at active lava lakes: implications for magma recycling. J Geophys Res 104:7117–7136
Harris AJL, Murray JB, Aries SE, Davies MA, Flynn LP, Wooster MJ, Wright R, Rothery DA (2000b) Effusion rate trends at Etna and Krafta and their implications for eruptive mechanisms. J Volcanol Geotherm Res 102:237–269
Harris AJL, Pilger E, Flynn LP, Garbeil H, Mouginis-Mark PJ, Kauahikaua J, Thornber C (2001) Automated, high temporal resolution, thermal analysis of Kilauea volcano, Hawaii, using GOES satellite data. Int J Remote Sensing 22(6):945–967
Harris AJL, Rothery DA, Carlton RW, Langaas S, Mannstein H (1995a) Non-zero saturation of AVHRR thermal channels over high temperature targets: evidence from volcano data and a possible explanation. Int J Remote Sensing 16(1):189–196
Horne R, Papathanassiou KP, Reigber A, Hausknecht P, Strobl P, Boehl R, Scheele M, Reulke R, Baerwald W, Puglisi G, Coltelli M, Fornaro G (1997) The Mount Etna case study: a multisensor view. 3rd International Airborne Remote Sensing Conference and Exhibition, 7–10 July 1997, Copenhagen
Harris AJL, Swabey SEJ, Higgins J (1995b) Automated thresholding of active lavas using AVHRR data. Int J Remote Sensing 16(18):3681–3686
Lombardo V, Buongiorno MF, Merucci L, Pieri DC (2004) Differences in Landsat TM derived lava flow thermal structure during summit and flank eruption at Mount Etna. J Volcanol Geotherm Res 134(1–2):15–34
Matson M, Dozier J (1981) Identification of subresolution high temperature sources using a thermal IR sensor. Photogramm Eng Remote Sensing 47(9):1311–1318
Mouginis-Mark PJ, Garbeil H, Flament P (1994) Effects of viewing geometry on AVHRR observation of volcanic thermal anomalies. Remote Sensing Environ 48:51–60
Oppenheimer C (1998) Satellite observation of active carbonatite volcanism at Ol Dionyo Lengai, Tanzania. Int J Remote Sensing 19:55–64
Oppenheimer C, Francis PW (1997) Remote sensing of heat, lava, and fumarole emissions from Erta 'Ale Volcano, Ethiopia. Int J Remote Sensing 18:1661–1692
Oppenheimer C (1997a) Remote sensing of colour and temperatures of volcanic lakes. Int J Remote Sensing 18:3–37
Oppenheimer C (1997b) Crater lake heat losses estimated using remote sensing. Geophys Res Lett 23:1793–1796
Oppenheimer C, Francis PW, Rothery DA, Carlton RWT, Glaze L (1993a) Infrared image analysis of volcanic thermal features: Làscar Volcano, Chile, 1984–1992. J Geophys Res 98:4269–4286
Oppenheimer C, Rothery DA, Francis PW (1993b) Thermal distribution at fumarole fields: implications for infrared remote sensing of active volcanoes. J Volcanol Geotherm Res 55:97–115
Oppenheimer C, Rothery DA, Pieri DC, Abrams MJ, Carrere V (1993c) Analysis of Airborne Visible/Infrared Imaging Spectrometer (AVIRIS) data of volcanic hot spots. Int J Remote Sensing 14(16):2919–2934
Oppenheimer C (1993a) Infrared surveillance of crater lakes using satellite data. J Volcanol Geotherm Res 55:117–128
Oppenheimer C (1993b) Thermal distributions of hot volcanic surfaces constrained using three infrared bands of remote sensing data. Geophys Res Lett 20(6):431–434
Oppenheimer C (1991) Lava flow cooling estimated from Landsat Thematic Mapper infrared data: the Lonquimay eruption (Chile, 1989). J Geophys Res 96:21865–21878
Oppenheimer C, Rothery DA (1991) Infrared monitoring of volcanoes by satellite. J Geol Soc Lond 148:563–569
Pieri DC, Glaze LS, Abrams MJ (1990) Thermal radiance observation of an active lava flow during th June 1984 eruption of Mt. Etna. Geology 18:1018–1022
Rothery DA, Oppenheimer C, Bonneville A (1995) Infrared thermal monitoring. In: McGuire B, Kilburn CRJ, Murray J (eds) Monitoring active volcanoes, UCL, London, pp 184–216
Rothery DA, Borgia A, Carlton RW, Oppenheimer C (1992) The 1992 Etna lava flow imaged by Landsat TM. Int J Remote Sensing 13:2759–2763
Rothery DA (1992) Monitoring and warming of volcanic eruptions by remote sensing. In: McCall GJH, Laming DJC, Scott SC (eds) Geohazards: natural and man-made, Chapman, New York, pp 25–32
Rothery DA, Francis PW, Wood CA (1988) Volcano monitoring using short wavelength infrared data from satellite. J Geophys Res 93:7993–8008
Swanson DA, Duffield WA, Jackson DB, Peterson DW (1979) Chronological narrative of the 1969–1971 Mauna Ulu eruption of Kilauea volcano, Hawaii. Geol Surv Prof Pap: 1056 pp 1–55
Tanguy JC (1973) The 1971 Etna eruption: petrography of lavas. Philos Trans Roy Soc London 274:45–53
Wan Z, Dozier J (1989) Land-surface temperature measurement from space: physical principles and inverse modelling. IEEE T Geosci Remote Sensing 27:268–277
Wooster MJ, Kaneko T, Nakada S, Shimizu H (2000) Discimination of lava dome activity styles using satellite-derived thermal structurs. J Vulcanol Geotherm Res 102:97–118
Wooster MJ, Rothery DA (1997a) Time series analysis of effusive volcanic activity using the ERS along track scanning radiometer: the 1995 eruption of Fernandina volcano, Galapagos Island. Remote Sensing Environ 69:109–117
Wooster MJ, Rothery DA (1997b) Thermal of Lascar volcano, Chile using infrared data from the along track scanning radiometer: a 1992–1995 time series. Bull Volcanol 58:566–579
Wright R, Flynn PF, Harris AJL (2001) Evolution of lava flow-fields at Mount Etna, 27–28 October 1999, observed by Landsat 7 ETM+. Bull Volcanol 63:1–7
Wright R., Rothery DA, Blake S, Pieri DC (2000) Improved remote sensing estimates of lava flow cooling: a case study of the 1991–1993 Mount Etna eruption. J Geophys Res 105:681–623